Journal of Materials Chemistry B

ROYAL SOCIETY OF CHEMISTRY

PAPER

View Article Online
View Journal | View Issue

Check for updates

Cite this: J. Mater. Chem. B, 2026, 14, 719

Supramolecular self-assemblies of Ru(II) phototherapeutics: biological activity of micro- and nano-particles acting as reservoirs

Jérôme Laisney, †[b] Sarah M. Kriger,†[a] Dmytro Havrylyuk,[a] Jason M. Unrine, [cd] David K. Heidary[a] and Edith C. Glazer *[a]

Received 3rd August 2025,
Accepted 26th November 2025

DOI: 10.1039/d5tb01785h

rsc.li/materials-b

Ruthenium(II) coordination complexes have many appealing properties as prodrugs, but can suffer from poor aqueous solubility and short circulation times, drastically decreasing efficiency *in vivo*. Nanoformulations using a variety of carriers, such as inclusion in polymers/lipids or adsorption on inorganic nanoparticles have been applied to overcome this limitation, but unfortunately, these approaches raise additional concerns regarding the fate of the carriers, with potential long-term toxicity and accumulation in vital organs. Here, we present an alternative delivery strategy with formation of pure and polymer-supported supramolecular self-assemblies of Ru(II) complexes acting as "reservoirs". A facile preparation of size-controlled particles was achieved using a controlled precipitation method, and the approach was validate using $[Ru(bpy)_3](PF_6)_2$ (bpy: 2,2′-bipyridine) and $[Ru(bpy)_2(dmbpy)](PF_6)_2$ (dmbpy: 6,6′-dimethyl-2,2′-bipyridine) as agents for photodynamic therapy (PDT) and photoactivated chemotherapy (PACT). Negatively-charged particles ranging from tens of nanometers to micron scale were obtained by controlling just temperature and precipitation in the presence of confining polymers. Dissolution rate, biological activity, cellular uptake, and localization were evaluated *in vitro* in the dark or after light activation and revealed the progressive dissolution of the particles, associated with a gradual and sustained cellular uptake compared to the soluble molecule form. Leveraging the ability of the $[Ru(bpy)_3]$ to act as a $^1O_2$ photocatalyst for deposition of an osmiophilic polymer, electron microscopy was performed and illustrated the delivery of the dissolved complex inside the nucleus of cells. These results open new possibilities for the pure micro- or polymer-supported nano- formulation of Ru-based compounds, and provide a strategy for evaluation of subcellular localization using electron microscopy.

Introduction

Nanotechnology offers opportunities for major advances in drug delivery, as nanomaterials provide specific properties that can help to overcome long-standing obstacles to success for small molecule drugs. These properties include an intrinsic size that may avoid rapid excretion, but still enabling cellular uptake; a high surface/volume ratio; and the possibility of surface functionalization for passivation, drug loading, and targeting.[1,2] These features can be advantageous for ruthenium (Ru(II)) polypyridyl complexes, which have been explored for application in chemotherapy but often suffer the drawbacks of low circulation time in the body, and lack of biocompatibility or targeting to specific tumor sites.[3–5] Intensive research efforts are underway to develop delivery systems to improve these properties.[6] The main strategies rely on the incorporation of Ru(II) complexes in nanomaterials such as polymers,[7–9] liposomes[10,11] or inorganic nanoparticles (NPs), including selenium NPs,[12] silica NPs,[13,14] gold NPs,[15–17] carbon nanodots,[18] carbon nanotubes,[19] or graphene oxide.[20] These nanosystems act as carriers to deliver and then release the metal complex to the site of action, and also enhance the bioavailability and pharmacokinetics properties of Ru compounds. The different nanoformulations have been shown to provide benefits in terms of targeting, cellular uptake, and efficacy, compared to the unformulated drug form.[21] However, the use of carriers, particularly inorganic particles, raises important questions concerning the fate of such materials after injection, and their possible accumulation in organs (lungs, kidney, spleen, liver, or brain) that could lead to potential long term toxicity.[22,23]

As an alternative, we have implemented a method of delivery that does not involve the use of extrinsic carriers. Ruthenium

[a] Department of Chemistry, North Carolina State University, 2620 Yarbrough Dr, Raleigh, NC, 27607, USA. E-mail: eglazer@ncsu.edu
[b] Department of Chemistry, University of Kentucky, 505 Rose St., Lexington, KY, 40506, USA
[c] Department of Plant and Soil Science, University of Kentucky, Lexington, KY, 40546, USA
[d] Kentucky Water Research Institute, University of Kentucky, Lexington, KY, 40506, USA
† Authors contributed equally.

complexes have been shown to undergo spontaneous self-assembly to form nanoparticles by precipitation in aqueous medium because of their strong hydrophobic character.[24] Several studies have reported the self-assembly of Ru complex particles[25–30] but, to the best of our knowledge, none have deeply investigated and rationalized the biological activity of such nanoaggregates according to their size, charge, shape and composition. Potentially, such controlled particles of Ru(II) complex would allow for (i) improved delivery to cells and endosomal escape, due to the highest density of charges present in the nanoparticulate form; (ii) controlled release of the Ru(II) complex over time through slow dissolution of nanoparticles; (iii) increased transport and retention time *in vivo*; and (iv), the possibility of surface functionalization to improve targeting and reduce toxicity. Here we show the careful control and reproducible generation of size-controlled micro- and nanoparticles through a fast precipitation (FP) technique. This bottom-up approach, which relies on the formation and growth of nuclei, is well suited for molecular materials such as coordination complexes as it allows for the controlled precipitation of solubilized precursors in solution, and even in the presence of a confining agent, by combination of appropriate solvent/anti-solvent conditions (Fig. 1A).[31] FP has been used previously to prepare size-controlled particles of Fe(II)[32,33] and Fe(III)[34] hybrid organic–inorganic materials. Due to the similar physio-chemical properties shared by Fe and Ru, we believed that this technique could be successfully applied to Ru(II) polypyridyl complexes to form size-controlled particles of Ru-based theranostic agents.

In this study, we compare and contrast the efficacy of photoactive Ru-based compound in the form of micro- and nanoparticles *vs.* soluble small molecules in the application of photodynamic therapy (PDT) and photoactivated chemotherapy (PACT). Size-controlled particles of Ru(II) coordination complexes were generated using FP with the prototypical complex, $[Ru(bpy)_3](PF_6)_2$ (bpy: 2,2′-bipyridyl) (compound **1**, Fig. 1B),[35] and a derivative, $[Ru(bpy)_2(dmbpy)]^{2+}$ (dmbpy: 6,6′-dimethyl-2,2′-bipyridine) (compound **2**, Fig. 1C). These two compounds exhibit cytotoxicity against cancer cell lines after light activation but work by different mechanisms: compound **1** catalytically generates singlet oxygen ($^1O_2$) and can be considered an example of a PDT agent, while **2** releases a ligand from the metal center, and thus functions *via* PACT.[36] By varying experimental parameters, particles were made from these complexes that ranged in size from tens of nanometers to several microns. The particulate forms do not inhibit the biological activity of the photoactive compound; on the contrary, they exhibit similar or enhanced *in vitro* anticancer properties compared to the soluble molecules.

Variations were observed for PDT or PACT due to the dissolution of the particles after light activation, leading to the release of active species directly inside cells and within the nucleus in a more progressive manner than the unformulated soluble complex. Detection of subcellular localization of compound **1** can be challenging, so to observe spatial distribution of the photocatalyst,[37–39] we utilized a technique for subcellular imaging *via* electron microscopy. This approach relies on the generation of $^1O_2$, which induces the oxidation of diaminobenzene, creating polymer deposits which may be stained with osmium and imaged, providing high resolution cellular details. This strategy has been applied with organic and protein-based photocatalysts in the past, and here we have extended the approach to a Ru(II) photosensitizer. This provides a method for indirect imaging of the subcellular localization of the photosensitizer *via* visualization of the osmium-stained polymer deposition that can be observed using electron microscopy. As a result, this report provides a simple and generalizable method to synthesize hybrid organic–inorganic particles, as well as a process to observe the localization of inorganic photocatalysts in sub-cellular regions. The promising results presented here are a step toward the nanoformulation of more effective, long-lasting anticancer metallodrugs-based treatments.

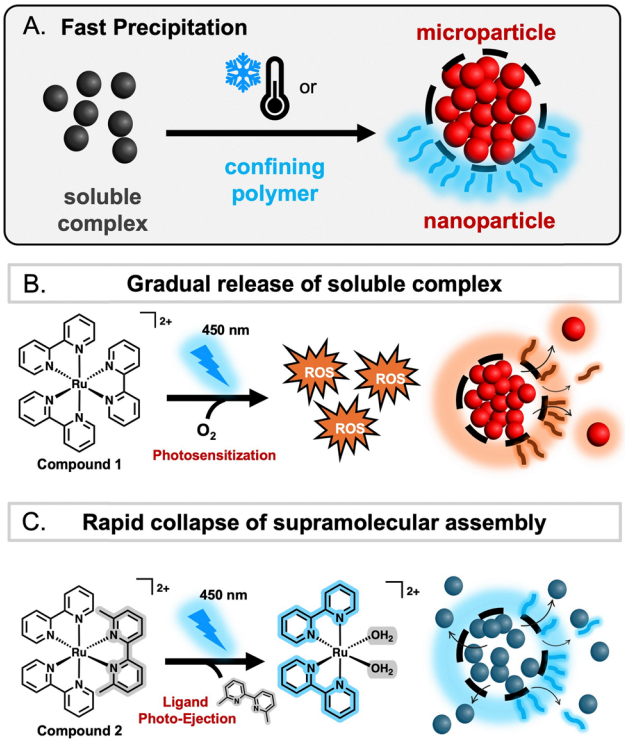

Fig. 1 Particle formulation and controlled release of Ru molecules. (A) FP using controlled temperature or the presence of a confining polymer to create particles on the micro- and nanoscale. (B) $[Ru(bpy)_3]^{2+}$ (compound **1**) is a PDT agent and (C) $[Ru(bpy)_2(dmbpy)]^{2+}$ (compound **2**) is a PACT agent, where photo-release of a ligand from the metal center causes collapse of the supramolecular assembly.

Materials and Methods

Chemicals and instruments

Cis-Dichlorobis(2,2′-bipyridine)Ruthenium(II) dihydrate (99% purity, Strem Chemicals Inc., Newburyport, MA, USA), 6,6′-dimethyl-2,2′-bipyridine (dmbpy, 98% purity, Sigma-Aldrich, Saint-Louis, MO, USA), 2,2′-bipyridyl (bpy, 99% purity, Sigma-Aldrich), potassium hexafluorophosphate (99%, Alfa Aesar, Haverhill, MA, USA), ethylene glycol (Sigma-Aldrich, 99% purity), acetonitrile (spectrophotometric grade, >99.5%, Acros Organics, Thermo Fisher Scientific, Waltham, MS, USA), 1-butanol (HPLC

grade, Acros Organics), pentane (VWR Chemicals), polyvinylpyrrolidone 10 kDa (PVP10, Sigma-Aldrich) or 55kDa (PVP55, Sigma-Aldrich), polyethylene glycol 6kDa (PEG6000, Sigma-Aldrich) were purchased and used without any further purification. Complexes syntheses were performed in a CEM Discover 2.0 microwave reactor (CEM, Matthews, NC, USA). The purity of the compounds was verified by high-performance liquid chromatography (HPLC) using an Agilent 1100 series (Agilent Technologies, Santa Clara, CA, USA). UV-vis spectra were collected using a Cary 60 spectrophotometer (Agilent Technologies, Santa Clara, CA, USA) equipped with a model G1311A quaternary pump, G1315B UV diode array detector and Chemstation software version B.01.03. FTIR spectroscopy was performed on the isolated powders using a Thermo Scientific Nicolet 7500 (Agilent Technologies, Santa Clara, CA, USA) operated in ATR mode (64 scans, 4 cm^{-1} resolution). Morphology (size, shape, and composition) of the prepared micro- and nanoparticles were observed using a TALOS F200X analytical electron microscope (Thermo Scientific, Waltham, MA, USA), operated at 200 keV and equipped with a four-element silicon drift detector (SDD)-based energy dispersive X-ray spectroscopy (EDS) system for quantitative chemical composition analysis and elemental distribution mapping. Zeta potentials in 1× PBS buffer (pH 7.4) were measured by phase analysis light scattering (PALS) with a Nano-ZS zetasizer (Malvern Instruments, Malvern, UK) using the Hückel approximation used to estimate zeta potential from electrophoretic mobility.

Synthesis of $[Ru(bpy)_3](PF_6)_2$ (1) and $[Ru(bpy)_2(dmbpy)](PF_6)_2$ (2) complexes

The synthesis of the Ru(II) complexes was adapted from a previously described procedure.[40] Briefly, 500 mg of $Ru(bpy)_2Cl_2{\cdot}2H_2O$ and 164.9 mg of 2,2′-bipyridine (for compound **1**) or 195 mg of 6,6′-dimethyl-2,2′-bipyridine (for compound **2**) were added to a 35 mL Pyrex reaction vessel with 20 mL of ethylene glycol. The purple reaction mixture was heated at 190 °C for 1h in the microwave reactor (300 W). The red solution was then added to 100 mL of deionized (DI) water and the PF_6 salt was precipitated by adding 6–8 mL of a saturated solution of KPF_6. The precipitates were collected by filtration, washed with cold water, diethyl ether, and dried under vacuum and stored in the dark at room temperature. Purification of the compounds was carried out with a silica gel column chromatography (eluent: 99% acetonitrile, 1% H_2O ramped to 16%, 0.1% KNO_3). The pure fractions were concentrated under reduced pressure, and the precipitation of the PF_6 form by adding a saturated solution of KPF_6 to the solution of the metal complex in water. The resulting polycrystalline powders were stored in the dark at room temperature. Yield: 90% (**1**), 85% (**2**). Purity: 99% (**1**), 97% (**2**) (see Fig. S1 in SI for HPLC chromatogram). Characteristic IR vibration bands: 552 and 826 cm^{-1} (υ PF_6^-, both **1** and **2**), 1389 cm^{-1} (υ CH_3, **2**), 1465, 1445 and 1422 cm^{-1} (pyridine vibration bands, both **1** and **2**), 1600 cm^{-1} (υ aromatic C–C, both **1** and **2**) (see Fig. S2).

Counter-ion exchange

For evaluation of the soluble complexes, compounds **1** and **2** were converted from PF_6^- salts to Cl^- salts by dissolving 10–50 mg of each complex in 1–2 mL of methanol. The dissolved compound was loaded onto an Amberlite IRA-410 chloride ion exchange column, eluted with methanol, and solvent was removed *in vacuo*.

Preparation of microparticles by FP

Ten milligrams of the Ru(II) complex were dissolved in 0.5 mL of acetonitrile (for precipitation at 0 °C) or 1 mL of acetone (for precipitation at −75 °C). The solution was added quickly to a 250 mL Erlenmeyer flask containing 20 mL of 1-butanol, which acts as the anti-solvent. The mixture was maintained at 0 °C in an ice bath or at −75 °C in a bath containing a mixture of dry ice and acetone. This mixture is commonly used for performing reactions at −78 °C. The temperature is reported here as −75 °C as the temperature of the cooling bath was carefully monitored using a thermometer, and very particular attention was given to maintaining this temperature and vigorous stirring during the reaction time, keeping in mind the increasing viscosity of the solution as the freezing point of butanol was approached. After 15 min, the precipitation process was stopped by centrifuging the solution at maximum speed for 10 min using a 5430R Eppendorf centrifuge (Eppendorf, Hamburg, Germany). The supernatant was discarded and the precipitated powder washed three times with pentane, with centrifugation at maximum speed for 5 min. The collected microparticle powders were stored at room temperature in the dark or aliquoted in PBS buffer (redispersion of around 5 mg in 500 μL of PBS) and then stored immediately at −20 °C until further characterizations.

Preparation of nanoparticles by FP using a confining agent

To reach the nanoscale level, precipitation was triggered in presence of a polymer acting as confining agent. Two hundred mg of polymer (PEG6000, PVP10, PVP55) was dissolved in 20 mL of butanol. The concentrated solution of the Ru complex (10 mg, dissolved in 0.5 mL of acetonitrile) was then added at room temperature to the butanol–polymer mixture under vigorous stirring. After 15 min, the solution was filtered through a sterilized 0.45 μm MCE membrane (Argos Technologies, Cole-Parmer, Vernon Hills, IL, USA). The particle-polymer composite was precipitated by cooling down the filtered solution in an ice bath (PEG6000 composite) or by addition of 150 mL of pentane (PVPs composite). The composite powders were then collected by centrifugation (maximum speed for 10 min) and washed multiple times with pentane. The powders were stored at room temperature in the dark or dispersed in PBS buffer (around 100 mg of composite dissolved in 0.5 mL of PBS) for immediate storage at −20 °C.

Dissolution rate of the particles in PBS medium

The stability of the particles in PBS buffer either kept in the dark or light-activated (1 min exposure to Indigo LED flood array, Loctite, $\lambda \sim 450$ nm, 29.1 J cm^{-2}) was investigated by dialysis using Float-A-Lyzer® dialysis devices (Repligen, Waltham, MA, USA) with molecular weight cut-off membranes of 8–10 kDa and a working volume of 1 mL. Experimentally, around 1 mg mL^{-1} of particles were suspended in PBS then loaded in the membrane previously prepared following the instruction of the manufacturer. In the case

of the complexes, the samples were prepared by dissolving the powder in methanol with the addition of a few drops of acetonitrile to improve solubilization. The different solutions were dialyzed at 37 °C in DI water as dialysate. Ten microliters of samples were pipetted from the dialysis device at different time points (t = 0 h, 2 h, 4 h, 16 h, 24 h, 48 h, 72 h) then added to 10 μL of acetonitrile in order to fully dissolve the particles. The ruthenium complex concentration in the different samples was then measured according to the absorbance at λ = 453 nm. The UV-Vis spectra were collected using a Varian Carry Bio 50 spectrometer (Agilent Technologies, Santa Clarita, CA, USA), by dropping 1 μL of sample on a tray cell (Hellma, Plainville, NY, USA; optical path = 1 mm or 0.2 mm).

Determination of the Ru(II) complex concentration in the DMSO stocks and PBS particle suspensions

The concentration of the Ru(II) complex in DMSO stock solutions or dispersed particles in 1× PBS (pH 7.4) was determined by UV-Vis spectroscopy by measuring the absorbance at 453 nm (MLCT band, ε (compound **1**) = 14 890 M^{-1} cm^{-1}, ε (compound **2**) = 13 780 M^{-1} cm^{-1}). The measurement was performed in acetonitrile by adding 10–50 μL of the solution of the complex or particle suspensions to 2 mL of acetonitrile to ensure the complete dissolution of the particles and the full release of the constituent small molecules.

Cytotoxicity assays

HL60, HeLa, A549, and HEK cells were plated in extracellular buffer at 30 000 or 2000 cells per well for suspended or adherent cells, respectively, in a 96 well flat bottom transparent microplate (Greiner Bio-One). Compounds were serial diluted in extracellular buffer with a 1 : 3 ratio and added to the cells such that the final concentration ranged from 0–100 μM. The cells were then incubated for 1 hour at 37 °C. Photoactivation was then carried out with an Indigo LED flood array (Loctite, ~450 nm, 29.1 J cm^{-2}) with a total light exposure time of 1 minute. Following this, OptiMEM supplemented with 4% FBS and 50 U mL^{-1} penicillin/streptomycin was added to all wells, and the cells were returned to the incubator. After 72 hours, resazurin was added and the plate was incubated for an additional 3 hours at 37 °C. The fluorescent intensity was read on a SpectraFluor Plus plate reader (Tecan) with an excitation filter of 535 nm and emission of 595 nm. Dark controls were run in parallel. The data was normalized to the untreated cells control and fitted to a sigmoidal dose response equation using GraphPad Prism 9 (GraphPad Software, San Diego, CA, USA) to determine the EC_{50} values.

Cellular association by ICP-MS

HeLa or A459 cells were seeded at a density of 2×10^5 cells per mL in 6 well plates and grown overnight in DMEM containing 10% FBS, 100 U penicillin and 100 μg mL^{-1} streptomycin at 37 °C with 5% CO_2. Cells were then incubated with 24 μM of complex **1**, or the particles (1.6 μm, 0.8 μm, 40 nm PVP10, or 20 nm PEG) diluted in extracellular solution. After 1 hour the cells were irradiated with indigo light for 1 minute using a 450 nm Loctite Flood Array with 144 individually reflectorized LEDs (item No. 1167593; regulated by an LED Flood System Controller, item No. 1359255) or kept in the dark. Opti-MEM containing 4% FBS was added and the cells were incubated for 72 hours. Following incubation, the cell medium was transferred to 15 mL centrifuge tubes. Cells were washed twice with PBS, trypsinized, and pelleted by centrifugation at 1000×g for 10 minutes in separate 15 mL tubes. Cell pellets and 1/25 fractions of the cell medium were digested with 150 μL of concentrated nitric acid (HNO_3), 50 μL of cold hydrogen peroxide (H_2O_2), and heated to 100 °C for 1 hour. Then 50 μL of hydrochloric acid (HCl) was added, samples were heated to 100 °C for 15 minutes, and volume was adjusted to 5 mL with DI water. The metal content was analyzed using an inductively coupled plasma mass spectrometer equipped with octopole reaction system with the octopole operated in standard mode (ICP-MS; Agilent 7500cx, Santa Clara, CA, USA). National Institute of Standards and Technology (NIST) trace-able external matrix matched standards for Ru were used and all samples and standards contained 10 ug L^{-1} In as an internal standard. Monitored masses were m/z 101 and 102 for Ru and m/z 115 for In. The acceptance criteria for the calibration curve was an observed concentration +/− 10 of the expected concentration of an independent standard from a different lot. Spike recovery, procedural blanks, and replicates were evaluated using randomly selected samples throughout the analytical run. The cellular association (in %) was calculated according to the formula:

$$\%\ \text{Cell association} = (\text{Ru found in the cell pellets}/\text{total amount of Ru in cell pellets and medium}) \times 100$$

The cellular association values were determined for different treatments to compare dark *vs.* photo-activated, and soluble molecules *versus* particles.

Cell culture and treatment for fluorescence microscopy

HeLa cells were cultured at 37 °C, 5% CO_2 in Dulbecco's modified Eagle medium (DMEM) supplemented with 10% Fetal Bovine Serum (FBS) and 100 U penicillin and 100 μg mL^{-1} streptomycin. Cells were seeded at 1×10^6 cells in 6-well plates containing poly-D-lysine treated Zeiss high-performance #1 $\frac{1}{2}$ glass cover slips and incubated overnight. PBS solutions of Ru particles were added to the cell extracellular solution at a final concentration of 20 μM. The cells were then incubated with the particles for 1 hour followed by irradiation for 1 minute using a 450 nm Loctite Flood Array with 144 individually reflectorized LEDs (item No. 1167589; regulated by an LED Flood System Controller, item No. 1359255). Cells were counterstained with 5 μM DRAQ5 nuclear dye (Thermo Scientific, No. 62251). Samples were washed twice with extracellular solution in between each step and kept in Opti-MEM supplemented with 2% FBS until mounting on glass slides for imaging.

Imaging and quantification

Images were captured using a Zeiss Plan-Apochromat 63x/1.4 NA oil objective mounted on a Zeiss 880 upright confocal

microscope equipped with an airyscan detector and Zeiss Zen software. Particles of **1** were imaged using a 488 nm excitation laser line with DRAQ5 imaged using a 640 nm excitation laser line. Airyscan processing and quantification of $Ru(bpy)_3$ localization and intensity was performed using Zeiss Zen Blue 3.0. Regions of interest (ROI) were defined based on the 2.5D surface plot and pixel intensity values for each ROI were averaged to obtain the arithmetic mean intensity. Data are represented as a bar chart generated using PRISM GraphPad 9.3.1.

Cell culture and treatment for Seahorse MitoStress test

A549 cells were cultured at 37 °C, 5% CO_2 in Dulbecco's modified Eagle medium (DMEM) supplemented with 10% Fetal Bovine Serum (FBS) and 100 U penicillin and 100 μg mL^{-1} streptomycin. Cells were seeded at 2×10^4 cells per well in Seahorse XF 96-well plates (Agilent), set at room temperature for 1 hour to allow cells to settle, and incubated overnight. PBS solutions of Ruthenium particles were added to the cells in Opti-MEM supplemented with 2% FBS at two different concentrations based on cytotoxicity results. Treatment concentrations were selected from the 16-hour EC_{50} of compound **1** particles in A549 cells, a maximum dose of 100 μM, and an estimated EC_{50} to EC_{80} concentration of 10 μM for compound **2** particles in A549 cells. The particles were added to $n = 8$ replicates at each treatment concentration. The cells were then incubated with the particles for 16 hours. Following incubation, the medium was exchanged for extracellular buffer. The light plate was irradiated for 1 minute using a 450 nm loctite flood array with 144 individually reflectorized LEDs (item No. 1167589; regulated by an LED flood system controller, item No. 1359255) and the dark plate remained in the dark for the entirety of the experiment. Opti-MEM supplemented with 4% FBS was added to all samples.

Seahorse mitochondrial stress test and analysis

Medium was aspirated from the cells and replaced with Seahorse XF DMEM (pH 7.4) supplemented with 25 mM XF Glucose, 2 mM XF Glutamine, and 1 mM Pyruvate. The standard seahorse MitoStress Test was initiated and the inhibitors were injected as follows: oligomycin (1.0 μM final concentration) at 18 minutes, carbonyl cyanide-p-trifluoromethoxyphenylhydrazone (FCCP, 1.2 μM final concentration) at 36 minutes, and rotenone/antimycin A (1.0 μM final concentration) at 54 minutes. Hoechst 33342 (20 μM final concentration) was included in the final injection of rotenone/antimycin A in order to measure cell viability and normalize results across samples. Data was exported from the Seahorse Analytics program to PRISM GraphPad 9.3.1 for plotting and statistical analysis. Data were analyzed by one-way ANOVA followed by Dunnett's multiple comparisons test (*$p < 0.05$, **$p < 0.01$, ***$p < 0.001$, ****$p < 0.0001$; n.s. = not significant).

Cellular uptake and imaging by electron microscopy

Sample preparation and staining was adapted from a prior report.[41] A549 cells were seeded at 350 000 cells per well on a Costar 3506 well-plate and incubated for 24 hours at 37 °C with 5% CO_2 to reach 70–80% confluency. The cells were then exposed to solubilized complex or particles (20 μM) dispersed in PBS for 16 h then fixed in 3.0% paraformaldehyde/glutaraldehyde mixture in 0.2 M Sorensen's buffer (pH 7.2) for 45 min on ice. The cells were washed multiple times with 0.2 M Sorensen's Buffer and 5% sucrose and let sit for 5 min. The endogenous enzyme activity was then blocked with 50 mM potassium cyanide and 100 mM glycine in PBS for 1.5 h to eliminate 3,3′-diaminobenzidine (DAB) oxidation background that occurs as a consequence of mitochondrial respiration. The role of glycine is to reduce auto fluorescence and background DAB precipitation and to prevent compound diffusion from the cells during the incubation step. The cells were washed three times with tris buffered saline (TBS, pH 7.4) followed by 2 mL of oxygen enriched 2 mg mL^{-1} DAB solution in TBS. The samples were photobleached and the DAB photo-polymerized by irradiating the plate 3 min with Indigo (450 nm) then 3 min with 405 nm light at maximum power. After washing with Sorensen's buffer, the cells undergone dehydration, resin infiltration (LX-112 resin) and staining (Osmium tetroxide, uranyl acetate). The resin blocks were ultra-microtomed and 90 nm thin sections were finally mounted on 300 mesh formvar gold grids.

Results and Discussion

Preparation of microparticles and nanoparticles of $[Ru(bpy)_3](PF_6)_2$ by FP

In previous work, FP was used to generate size-controlled particles from complexes of Fe(II)[32,33] and Fe(III).[34] To apply the FP technique to compound **1**, the complex was dissolved at a concentration close to saturation using a minimum volume of solvent. Acetonitrile was used for FP at temperature above −40 °C, and acetone for lower temperatures to prevent freezing. This solution was then added to a large volume of an anti-solvent, 1-butanol, to reach a saturated concentration of the complex, triggering nucleation and growth of nuclei in the reaction medium.[31] The growth of the particles was controlled using temperature by performing FP at 0 °C and −75 °C, and by the inclusion of two different confining agents, PEG or PVP polymers, in the anti-solvent. The particles were then isolated and suspended in PBS before characterization by transmission electron microscopy (TEM) and scanning transmission electron microscopy (STEM) to quantify the size distribution of the materials. High-angle annular dark-field (HAADF) images were obtained, and elemental mapping was performed by energy dispersive X-ray (EDS) spectroscopy of the particles to visualize C, N, O, P, F, and Ru, as shown in Fig. S9–S12.

When FP was performed at 0 °C, platelet shaped microparticles formed, with dimensions of 1.60 ± 0.78 μm in length, 0.52 ± 0.22 μm width, and 0.11 ± 0.05 μm height (Fig. 2A). Decreasing the temperature to −75 °C resulted in a 2-fold decrease in the length of the platelet (0.76 ± 0.42 μm) with a similar width (0.45 ± 0.20 μm) but increased height (0.24 ± 0.10 μm). This result agrees with LaMer's model describing the general mechanism of nucleation and growth.[42] Indeed, lower temperatures enhance supersaturation due to reduced solubility, favoring nucleation overgrowth and leading to smaller

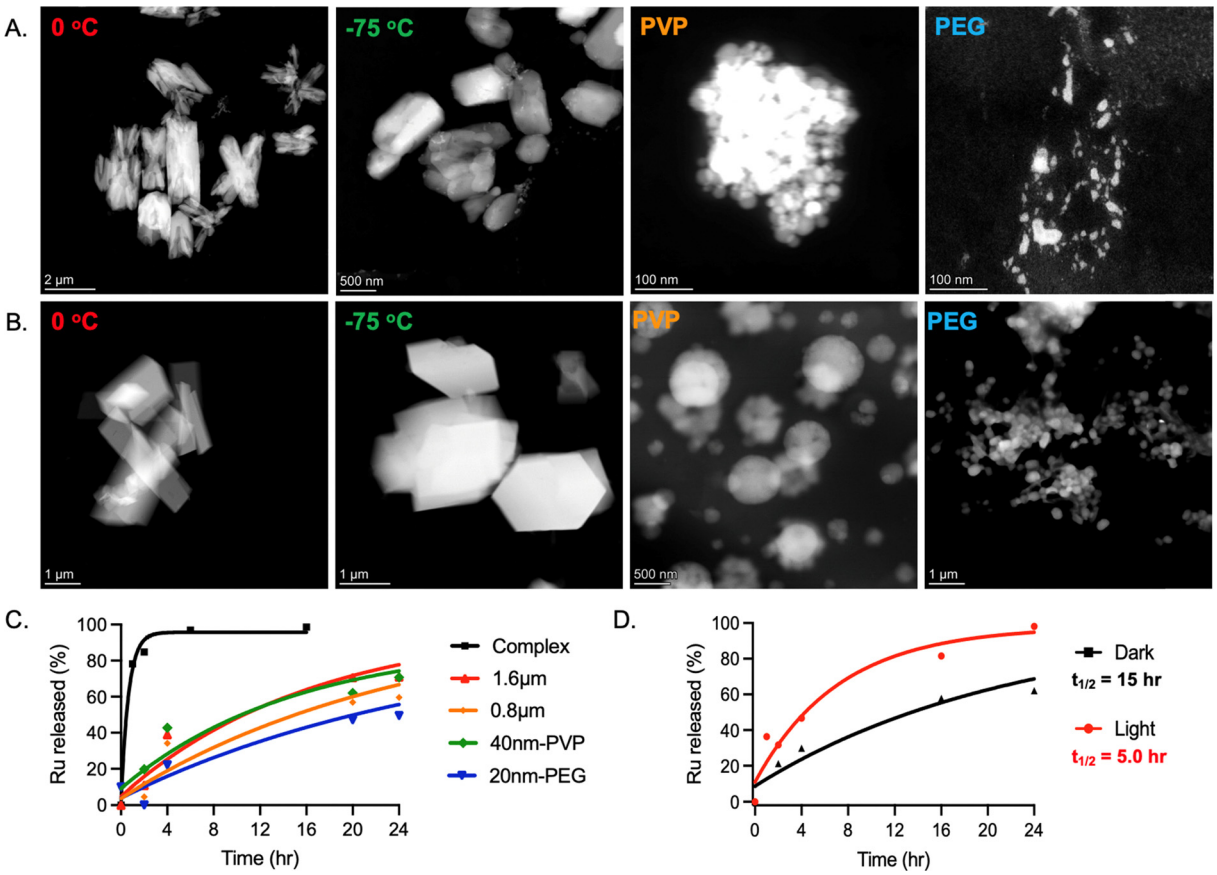

Fig. 2 High-angle annular dark field (HAADF) scanning transmission electron microscopy (STEM) images of (A) compound **1** and (B) **2** particle formulations. Different conditions were used, as indicated by the variation in temperature (0, −75 °C) and the inclusion of confining agents (PVP, PEG). Time dependent release of (C) compound **1** particles in the dark and (D) 2.6 μm particles of compound **2** under dark and light conditions during dialysis in PBS. A MWCO membrane of 8–10 kDa was used, and the temperature was maintained at 37 °C. The soluble Ru(II) complexes were dissolved in methanol at 1 mg mL^{-1}, and the Ru(II) particles were suspended at 1 mg mL^{-1} in PBS. Samples were kept in the dark or photo-activated (λ = 450 nm, t = 1 min, for a light dose of 29.1 J cm^{-2}).

particles formation. Simultaneously, decreased thermal energy and increased medium viscosity limit particle mobility (Brownian motion) and interaction, thereby slowing down coalescence and promoting the formation of uniformly smaller particles. Given the freezing points of acetone and 1-butanol (−95 °C and −89.6 °C, respectively) and the significant rise in medium viscosity near these temperatures, the system was cooled to the lowest experimentally feasible temperature. However, this approach did not yield particle sizes below 100 nm. Polymers were introduced as confining agents as a means to prevent the growth of the nuclei by introducing steric hindrance, thus allowing for size-controlled particle formation at the nanoscale. The polymers were dissolved in butanol prior to the addition of the saturated solution of the Ru(II) complex precursor, with a Ru(II) complex/polymer weight ratio ($W_{Ru}/W_{polymer}$) of 5 wt%. Polyethylene glycol (PEG) and polyvinylpyrrolidone (PVP) were selected because of their biocompatibility and degradability,[43,44] regular use in nanoparticles synthesis,[45–47] their previous use for controlled precipitation,[33,34] and the stability that they provide in aqueous medium, which could increase the circulation time of drugs in the bloodstream.[48,49] In addition, PVP can adhere to different types of surfaces through multiple weak interactions mediated by its pyrrolidone groups, such as hydrogens bonds and van der Waals contacts, resulting in the formation of amorphous films.[50]

The encapsulation of Ru particles within the polymeric matrix hindered imaging by TEM. Switching to STEM in HAADF mode enabled clearer visualization of regions with highest electron density and thus disentangled the particles composed of ruthenium, phosphorus, and fluorine atoms from the confining polymers, composed of carbon and oxygen (Fig. S9–S12). FP at room temperature in the presence of PEG drastically decreased the particle size to 20 nm (Fig. 2A), and the nanomaterials possessed an elongated spherical shape with an average length of 21.8 ± 9.2 nm. The PVP particles had a clear spherical shape, with average diameters of 37.3 ± 11.2 nm and 21.6 ± 9.8 nm for PVP of 10 kDa and 55 kDa, respectively. Notably, the use of the highest molecular weight polymer, with the longest polymeric chains, decreased the particles diameter by inducing stronger steric hindrance to the nuclei. Polymer addition provided further steric stabilization by forming a physical barrier that inhibits particle interaction and aggregation, with the effect intensifying at higher molecular weights.

Polymers, particularly PVP, also increased medium viscosity, reducing molecular diffusion and limiting particle growth and coalescence as discussed previously. The smallest nanoparticles could be obtained either by increasing the molecular weight of the confining agent (MW > 50 kDa) or by decreasing the Ru/polymer weight ratio ($W_{Ru}/W_{polymer}$ < 5 wt%).

The elemental composition of the particles was analyzed using HAADF coupled with EDS, as shown in Fig. S9–S12. The results indicated the presence of C, N, O along with P, F, and Ru, elements characteristic of the $[Ru(bpy)_3](PF_6)_2$ compound. To further confirm their chemical nature, FTIR was performed on the complex used for FP, and compared to the particle/nanocomposite powders formed by FP and collected after centrifugation (Fig. S2). The spectrum of the polycrystalline powder corresponded well to the experimental and simulated spectra provided by DFT calculations of the $[Ru(bpy)_3]^{2+}$ complex reported in the literature.[51,52] Signals observed at 828 cm^{-1} and 552 cm^{-1}, which are associated with the asymmetric and symmetric vibrations of PF_6^-, respectively, were among the most intense and characteristic vibrational bands. The FTIR spectra of the microparticles matches well with those of the $[Ru(bpy)_3](PF_6)_2$ complex, confirming the controlled precipitation of $[Ru(bpy)_3](PF_6)_2$ particles. Minor changes in the relative intensity and patterns of some vibrational bands were observed. For example, one single peak observed at 763 cm^{-1} in the microparticles spectrum appeared as a doublet at 773 cm^{-1} and 758 cm^{-1} for the polycrystalline powder, which can possibly be attributed to the crystallites orientation (anisotropy) or pressure effect in Attenuated Total Reflectance (ATR) mode. The nanocomposite spectra of 5 wt% of Ru complex showed strong overlapping of the bands associated with the polymer, with vibrations modes of C=O, C–C, CH_2, C–N in the mid-IR range. Nevertheless, in the 800–600 cm^{-1} region where the polymers weakly absorb, a few markers of the complex can be observed, especially at 763 cm^{-1} and 731 cm^{-1}, corresponding to vibration modes of the pyridine aromatic rings, as well as at 553 cm^{-1}, reflecting the symmetric vibration of the PF_6^-.

The charge of the particles was evaluated by measuring the zeta potential (ζ) by Phase Analysis Light Scattering (PALS) of the particles in PBS medium (pH 7.4). The results indicated negatively charged particles at physiological pH, with an increasing net negative charge corresponding to a decrease in particle size, as shown in Table 1 ($\zeta = -12.2 \pm 7.7$ mV for 1.6 μm particles *vs.* -20.2 ± 11.6 mV for the 20 nm PEG particles). The increase of the net charge with reducing size can be associated with a higher density of charge on the surface, resulting from the highest surface/volume ratio for the smallest particles. As the zeta potential measures the electric potential between the surface and the electric double layer,[53] the origin of these negative charges could either be associated with the highest presence of PF_6^- counter-ions at the surface of the particles, buffer-related interactions of the supramolecular framework with the cationic Ru(II) complexes, or structural defects at the surface.

Preparation of microparticles and nanoparticles of photolabile $[Ru(bpy)_2(dmbpy)](PF_6)_2$ by FP

The FP technique was applied to compound **2** with the exact same conditions of temperature and weight ratio of confining agents (5 wt% Ru:polymer) as for compound **1**. This resulted in the formation of particles of similar shape (spheroids, platelets) but with larger sizes (300–2800 nm range) compared to **1**, as illustrated in Fig. 2. The size of the different particles and their properties are reported in Table 1. As with **1**, the charge of the particles measured by PALS was negative at physiological pH, with the net charge increasing as the size of the particles decreases. Particles prepared at 0 °C without any confining agent gave plates of 2.76 ± 0.95 μm length, 1.16 ± 0.45 μm width and 0.38 ± 0.20 μm thickness (Fig. 2B). Decreasing the temperature to −75 °C led also to the reduction by 2-fold of the platelet length (1.60 ± 45 μm) while the width and thickness remained nearly identical (1.12 ± 0.35 μm and 0.46 ± 0.20 μm, respectively).

The use of confining agents reduced the size of the particles, but was not sufficient to reach the nanoscale level. Spheroid-like particles exhibiting an intermediate morphology between a perfect sphere and a platelet of 380 ± 160 nm and 295 ± 75 nm diameters were formed with PVP55 and PEG, respectively. FTIR spectra and HAADF-EDS confirmed the formation of particles of the $[Ru(bpy)_2(dmbpy)](PF_6)_2$ compound (Fig. S2 and S13–S16).

Table 1 FP conditions applied to compounds **1** and **2**, and the properties of the particles. Zeta potential measured in 1× PBS buffer (pH 7.4). $t_{1/2}$: half-life for release; n.d.: not determined. The half-life for release was extracted for the different samples from fitting the experimental data using a one phase exponential decay function. (*) Each soluble complex of **1** and **2** are the chloride forms. The particles of each complex are made from PF_6 salt. (—) is not applicable

Sample	FP Temp.	FP polymer	Shape	Diameter (TEM)	Zeta potential (mV)	Dark $t_{1/2}$ (hours)	Light $t_{1/2}$ (hours)
Complex **1***	—	—	—	—	—	0.40	n.d.
1.6 μm	0 °C	—	Platelet	$1.60 \pm 0.78 \times 0.52 \pm 0.22 \times 0.11 \pm 0.05$ μm^3	-12.2 ± 7.7	14.0	11.4
0.8 μm	−75 °C	—	Platelet	$0.76 \pm 0.42 \times 0.45 \pm 0.20 \times 0.24 \pm 0.10$ μm^3	-16.7 ± 15.6	n.d.	16.9
40 nm	Ambient	PVP	Sphere	37.3 ± 11.2 nm	-14.9 ± 8.2	21.9	10.3
20 nm	Ambient	PEG	Sphere	21.8 ± 9.2 nm	-20.2 ± 11.6	17.4	17.5
Complex **2***	—	—	—	—	—	1.0	n.d.
2.6 μm	0 °C	—	Platelet	$2.76 \pm 0.95 \times 1.16 \pm 0.45 \times 0.38 \pm 0.20$ μm^3	-8.2 ± 6.0	15.3	5.0
1.8 μm	−75 °C	—	Platelet	$1.60 \pm 0.45 \times 1.12 \pm 0.35 \times 0.46 \pm 0.20$ μm^3	-41.0 ± 9.4	n.d.	8.0
380 nm	Ambient	PVP	Sphere	380 ± 160 nm	-10.6 ± 12.6	9.4	7.3
300 nm	Ambient	PEG	Sphere	295 ± 75 nm	-21.2 ± 6.2	9.7	1.4

Applying the same FP conditions used for compound **1** resulted in a more rapid growth rate for compound **2**, likely due to differences in solubility between the two compounds. The lower solubility of compound **1** under these FP conditions increases supersaturation, accelerating nucleation and producing a greater population of smaller particles. The preparation of small nanoparticles (<100 nm) of **2** required adjustments to the solvent/antisolvent couple, reduction of the stirring time, the use of polymers with highest molecular weight, or an increase of the Ru:polymer weight ratio. Nevertheless, it was possible to apply the FP technique to another Ru(II) complex to obtain size-controlled particles.

Supramolecular structure stability and dissolution of PDT particles in PBS medium

The stability and dissolution rates of the Ru(II) particles were investigated. Particle suspensions in PBS at 37 °C (~1 mg mL^{-1}) were dialyzed using an 8–10 kDa Molecular Weight Cut Off (MWCO) membrane to separate the dissolved species from the particles. The quantity of Ru complex inside the dialysis bag was evaluated over time by removing a small volume of the particle suspension, dissolving the particles in acetonitrile, and quantifying the absorbance at 453 nm. The UV-Vis spectra collected in the dark or after light irradiation are presented in Fig. S18 and S19, and the percentage of Ru(II) released was determined as shown in Fig. 2C. As a control, the solubilized complexes in methanol were subjected to the same conditions. As expected, the solubilized complex rapidly diffused through the dialysis bag ($t_{1/2}$ (complex) = 0.4 h) and migrated completely into the dialysate after less than 6 h. A slower release of Ru(II) complexes was observed for the particles; for 1.6 μm particles in the dark, $t_{1/2}$ = 14.0 h, and an almost complete release of the complex/dissolution of the particles was observed after 72 h. Notably, this corresponds to the incubation time used during the *in vitro* assays. The nanoparticles embedded in polymers exhibited a slower dissolution rate than the bare particles; for 40 nm PVP in the dark, $t_{1/2}$ = 21.9 h; for 20 nm PEG in the dark, $t_{1/2}$ = 17.4 h. This suggests that the polymers form a protective coating around the nanoparticles, prolonging their resistance to dissolution in the surrounding medium. Light irradiation of the particles slightly enhanced the dissolution rate of the particles. After light exposure, the 1.6 μm systems exhibited $t_{1/2}$ = 11.4 h; for 40 nm PVP, $t_{1/2}$ = 10.3 h. The exception was the particles coated with PEG, which exhibited very similar $t_{1/2}$ values both in dark and after light-exposure (20 nm PEG, light $t_{1/2}$ = 17.5 h). PEG is a semi-crystalline polymer and its presence on the surface or in the medium can diffract the light and decrease the light-activation efficiency.[54] From these data, we considered the particles as a reservoir of complexes organized in a crystalline supramolecular structure, releasing the photo-active molecules over time in a progressive manner. Furthermore, in contrast to small molecules, the release rate of the particles could be tuned either by modifying the polymeric coating and/or by changing the photo-irradiation parameters such as time or power.

Light-induced dissolution of PACT particles

The stability of compound **2** particles was studied using the same dialysis method as for **1**, both in the dark or following light exposure. The dissolution rate of the particles in the dark was similar for particles of both **1** and **2**, but it was anticipated that the irradiation of particles of **2** would cause a rapid collapse of the edifice resulting from the fragmentation of the metal complex. Indeed, the red-orange suspensions turned deep red with irradiation, indicative of the release of a dmbpy ligand and the generation of $[Ru(bpy)_2(H_2O)_2]^{2+}$ complexes. The UV-vis spectra of the suspensions collected during dialysis are shown in Fig. S20, and the percentage of Ru released over time and the extracted half-release times for the different samples are presented in Fig. 2D and Table 1. Light treatment drastically increased the release and dissolution rate of the particles, with $t_{1/2}$ values close to the soluble molecule form ($t_{1/2}$ < 8 h depending on the samples). The dataset confirms the more rapid collapse of the supramolecular structure with the departure of the photo-labile ligand as a result of photo-irradiation.

Anticancer activity of Ru(II) microparticles and nanoparticles

The *in vitro* anticancer activity of compound **1** microparticles and nanoparticles was evaluated in HL60, HeLa, and A549 cancer cell lines. Table 2 reports the EC_{50} values after treating the cells with the different formulations in the dark and upon exposure to light. No toxicity was observed related to the presence of the polymers (Fig. S27) within the concentration window used in the composite dispersions (5 w% Ru complex:-polymer). When the cells were incubated in the dark, no cytotoxicity was observed in all cell lines and formulations.

After light activation, the Ru(II) compounds displayed anticancer potential. Compound **1** possessed EC_{50} values of 1.1 μM,

Table 2 Cytotoxicity of soluble compound **1** and particles in HL60, HeLa, and A549 cell lines with no irradiation (dark) or indigo light (450 nm). EC_{50} values were determined after 72 hours of incubation with the various treatments, either in the dark or following 1 minute of irradiation using an indigo LED (λ = 450 nm, 29.1 J cm^{-2}). (n.d.) is not determined

	EC_{50} in HL60 cells (μM)		EC_{50} in HeLa cells (μM)		EC_{50} in A549 cells (μM)	
Samples	Dark	Light	Dark	Light	Dark	Light
Complex	>100	1.09 ± 0.10	>100	10.69 ± 1.4	n.d.	41.37 ± 10.1
1.6 μm	>100	0.65 ± 0.03	>100	5.64 ± 1.3	>100	8.23 ± 0.4
0.8 μm	>100	0.45 ± 0.07	>100	5.75 ± 4.1	>100	17.21 ± 5.7
40 nm PVP10	>100	1.18 ± 0.02	>100	15.88 ± 0.7	>100	34.3 ± 2.0
20 nm PVP55	>100	0.98 ± 0.20	>100	13.87 ± 1.6	n.d.	n.d.
20 nm PEG	>100	0.89 ± 0.01	>100	13.49 ± 4.4	>100	26.5 ± 1.9

10.7 μM and 41.37 μM in HL60, HeLa, and A459 cells, respectively. Interestingly, the micro- and nanoparticle forms do not inhibit the anticancer activity but on the contrary, exhibit similar or lower EC_{50} values compared to the soluble complex form. Enhanced potency occurred in the case of the uncoated 1.6 μm and 0.8 μm microparticles in all cell lines. In particular, >2-fold reduction of the EC_{50} was observed for the 0.8 μm microparticles (0.45 μM and 5.75 μM in HL60 and HeLa cells, respectively). The nanoparticles confined in polymers presented values similar to the soluble small molecules. This could be explained by an incomplete photo-activation due to the presence of the polymer either associated at the surface of the particles or in the medium, or by a less effective cellular internalization of the encapsulated nanoparticles. No significant differences between the PEG- and PVP-containing particles were noted.

Many photosensitizers localize or accumulate in the mitochondria because of electrostatic and hydrophobic properties. Upon light activation, PDT agents generate reactive oxygen species (ROS), particularly singlet oxygen ($^1O_2$), which are damaging to mitochondrial membranes, disrupt the electron transport chain, and trigger cell death.[55] The mitochondrial stress test (Seahorse MitoStress Test) measures mitochondria function by analyzing oxygen consumption rate (OCR) in live cells. It sequentially introduces compounds, including oligomycin, FCCP, and rotenone/antimycin A, to assess key parameters such as basal respiration, ATP production, maximal respiration, and spare respiratory capacity. For PDT agents, this test can determine how they affect mitochondrial health and bioenergetics,[55] revealing mechanisms of action related to oxidative phosphorylation, mitochondrial stress, or oxidative cellular dysfunction. The bioenergetics of A549 cells treated with both the soluble complex and the particle formulations was assessed using the Seahorse Mito Stress Test, under both dark and photoactivated (indigo light) conditions (Fig. S35). In the absence of light, neither the soluble complex nor the particles at tested concentrations significantly altered cellular respiration. Basal respiration, ATP production, and spare respiratory capacity remained comparable to untreated controls, indicating minimal mitochondrial toxicity in the dark. However, upon exposure to indigo light, a loss of mitochondrial function was observed across all treatment groups for compound **1** and particles. At both 100 μM and concentrations between the EC_{50} and EC_{80}, mitochondrial respiration was nearly abolished, as shown by a significant decrease in oxygen consumption rate (OCR). This suggests that both the free complex and micro-/nanoparticle formulations are highly effective at disrupting mitochondrial activity when photoactivated. The extent of inhibition suggests that the mitochondria are a primary target of the photosensitized damage, likely due to the generation of ROS. Moreover, the results suggest that nanoformulation does not impede ROS generation.

In contrast, compound **2** and its corresponding particles exhibited much smaller changes in OCR following light exposure. Samples treated with both 100 μM and concentrations between the EC_{50} and EC_{80} maintained basal respiration levels and caused only a minimal decrease in maximal respiratory capacity, indicating a substantially lower degree of mitochondrial disruption (Fig. S36). This is an expected result given that compound **2** is a PACT agent;[55] it functions primarily through DNA damage, not ROS production.[29]

The anticancer activity of complex **2** and particles were only evaluated in HL60 cells, as the compound showed no potency in HeLa cells (Fig. S41). HL60 cells were treated with each particle formulation for 1 hour prior to light activation and then incubated for an additional 72 hours before evaluating the cell viability (Tables 3 and 4). In the absence of light, the soluble complex exhibited no cytotoxicity, whereas the nanoparticle formulations displayed some dark toxicity as particle size decreased, particularly in the PEG- and PVP-based systems. The counterion of a metal complex can influence its solubility, stability, and interaction within the particle assembly, affecting how the complex is loaded, released, and distributed in

Table 3 Cytotoxicity comparison of soluble compound **2** and particles prepared from PF_6 and BF_4 precursors in HL60 cells with no irradiation (dark) or indigo light (450 nm). EC_{50} values were determined after 72 hours of incubation with the various treatments, either in the dark or following 1 minute of irradiation using an indigo LED (λ = 450 nm, 29.1 J cm^{-2}). Cytotoxicity dose responses were evaluated in triplicate and EC_{50} values were calculated using a sigmoidal regression. (*) Complex **2** is the solubilized chloride form. The particles of **2** were prepared from PF_6 or BF_4 salt precursors

	Compound 2 (PF_6)		Compound 2 (BF_4)	
Samples	Dark (μM)	Light (μM)	Dark (μM)	Light (μM)
Complex 2*	>100	1.21 ± 0.02	>100	1.05 ± 0.04
3.6 μm	>100	1.06 ± 0.10	>100	1.10 ± 0.01
2.8 μm	>100	1.35 ± 0.02	>100	1.08 ± 0.06
380 nm PVP	62.13 ± 15.1	0.88 ± 0.20	>100	0.97 ± 0.18
300 nm PEG	98.06 ± 1.2	1.29 ± 0.04	>100	1.10 ± 0.03

Table 4 Cytotoxicity (EC_{50}) values and zeta potentials of compound **2** particles post-functionalized with PLR, PLK, and PLO positively-charged polymers. EC_{50} values were determined after 72 hours of incubation with the various treatments, either in the dark or following 1 minute of irradiation using an indigo LED (λ = 450 nm, 29.1 J cm^{-2}). Cytotoxicity dose responses were evaluated in triplicate and EC_{50} values were calculated using a sigmoidal regression. All zeta potential values were measured in 1× PBS (pH 7.4)

	None		PLR		PLK		PLO	
Samples	ξ (mV)	Light EC_{50} (μM)	ξ (mV)	Light EC_{50} (μM)	ξ (mV)	Light EC_{50} (μM)	ξ (mV)	Light EC_{50} (μM)
3.6 μm	−7.0	1.68 ± 0.09	+11.4	1.11 ± 0.09	+15.4	1.14 ± 0.1	+15.1	1.24 ± 0.02
0.5 μm	−4.0	1.48 ± 0.04	+2.0	0.54 ± 0.02	+4.0	0.52 ± 0.03	+2.0	0.80 ± 0.24
250 nm	−10.9	1.35 ± 0.02	+20.7	1.27 ± 0.08	+10.2	1.17 ± 0.06	+4.4	1.43 ± 0.08

biological systems. These factors can impact cellular uptake and biological activity of the particle formulations and further demonstrate the tunability of this approach using counter ion selection.[56] To investigate this effect, particles derived from the BF_4 form of compound **2** – considered more soluble than the PF_6 analogue – were also evaluate. Notably, polymer-supported nanoparticles prepared from the BF_4 precursor exhibited no dark toxicity, in contrast to the PF_6 particles (Table 3), consistent with more complete dissolution. Upon light exposure, both the PF_6 and BF_4 particles demonstrated phototoxicity with EC_{50} values closely matching that of the soluble complex (Table 3). Notably, a slight enhancement in potency was observed for the PVP particles, with an EC_{50} of 0.88 μM and 0.97 μM, for PF_6 and BF_4 particles respectively. The similarity in EC_{50} values between the free complex and its particle-based formulations supports the conclusion that the particles fully dissolve upon irradiation, releasing the photo-labile ligand.

The cytotoxic effects of compound **2** and its nanoparticle formulations were also evaluated to determine the influence of surface charge and polymer composition on biological activity. The negatively-charged Ru particles were post-functionalized with polycationic polymers commonly used as transfecting agents, particularly for the delivery of nucleic acids.[57] By varying the type of polymer—specifically incorporating PLR, PLK, or PLO into the suspension—the net surface charge of the particles at physiological pH was modulated with zeta potentials ranging from +2 mV to +20.7 mV depending on the particle size and polymer used (Table 4). This allowed for examination of how surface properties impact cellular interactions and toxicity. Under photoactivation, all post-functionalized particle formulations exhibited lower EC_{50} values than the unmodified negatively-charged particles, suggesting improved cellular uptake. However, no clear correlation could be observed between EC_{50} and zeta potential values, mostly because of a notable increase in dark cytotoxicity for most of the particles modified with the cationic polymers (Fig. S30–32). This unintended toxicity in the absence of light points to possible off-target interactions driven by the surface properties of the particles, such as enhanced cellular uptake or membrane disruption caused by the positive charges.[58] Free polycations, *i.e.* not bound to the surface, may also interfere with accurate surface charge measurements, necessitating alternative approaches. Titrating the zeta potential of bare particles across varying pH and buffer conditions would allow the determination of the isoelectric point, enabling assessment of biological activity for positively and negatively charged particles while minimizing cytotoxicity and measurement artifacts from unbound polycationic species. The results highlight a trade-off between modulating surface characteristics to optimize delivery and the need to maintain biocompatibility in the dark. From the dissolution and cytotoxicity data, one fundamental question remained: whether the dissociation of the particles and the release of dissolved species occurred in the extracellular or intracellular environment.

Cellular association, accumulation, and localization of the compound 1 particles

Accumulation rate of the particles in the cells. The cellular association in HeLa cells exposed to 20 μM of compound **1** as a soluble molecule or in the particulate form was quantified by measuring the amount of Ru present in both the cell pellets (associated Ru) and incubation medium (unassociated Ru). The experimental conditions mimicked those used during the cytotoxicity assays and the net Ru content found in the cells after exposure are shown in Fig. 3. Ru was found in the

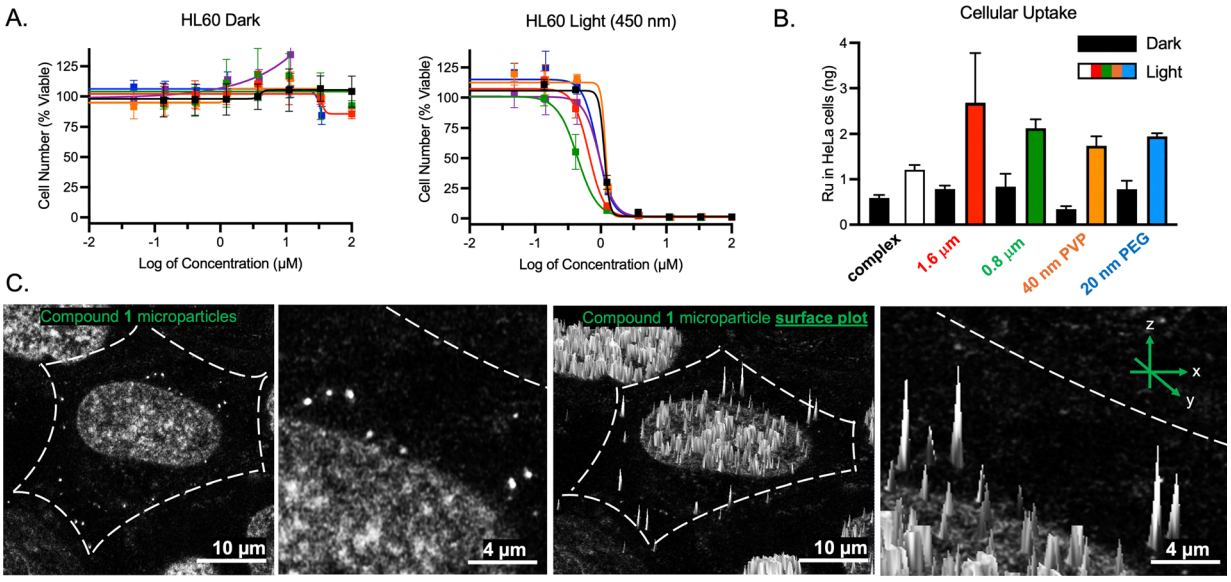

Fig. 3 Biological activity of compound **1** and particles in live cells. (A) Representative cytotoxicity plots of HL60 cells treated with **1** and particles in the dark and with indigo light exposure quantified after 72 hr incubation. (B) Quantification of Ru associated with HeLa cells at 72 hr by ICP-MS. The colors of the data plots for each condition for (A) match the colors for the conditions on the *x*-axis of the ICP-MS based association plot in (B). The one exception is the purple squares, which indicate PVP55. (C) Confocal microscopy of compound **1** microparticles in HeLa cells. The surface plot was used to illustrate the differences in signal intensity in different cell locations, with particles of **1** showing concentrated and more intense signal than the dissolved complex.

nanogram and microgram range in both the cell pellets and in the medium, respectively. Associated Ru was detected in the dark with similar values for the different treatments ($[Ru]_{(\mathbf{1}(Cl),\ dark)}$ = 0.054 ± 0.006%; $[Ru]_{(1.6\ \mu m,\ dark)}$ = 0.047 ± 0.005%; $[Ru]_{(20\ nm\ PEG,\ dark)}$ = 0.057 ± 0.013%). However, the PVP particles showed a lower amount compared to the other treatments ((40 nm PVP10, dark) = 0.029 ± 0.005%). Because PVP is a film-forming polymer, its presence in the medium could potentially prevent the cellular uptake of the nanoparticles by forming a polymeric film on the cells surface.

Notably, the amount of associated Ru with the cells significantly increased after light activation ($[Ru]_{(\mathbf{1}(Cl),\ light)}$ = 0.104 ± 0.009%; $[Ru]_{(1.6\ \mu m,\ light)}$ = 0.163 ± 0.066%; $[Ru]_{(40\ nm\ PVP10,\ light)}$ = 0.141 ± 0.017%, $[Ru]_{(20\ nm\ PEG,\ light)}$ = 0.134 ± 0.005%). The data also showed enhanced cellular association for the nanoparticles compared to the soluble complex, particularly when the particle size is small, which yielded the highest Ru content and percent association values. This improvement may be attributed to the higher net charges carried by the particles, resulting from electron transfer after photo-excitation within the MLCT band. The increase in charge, especially in the case of small nanoparticles, could enhance the potential for uptake by endocytosis or diffusion through the lipid bilayer membrane.[59] As demonstrated previously, the release of Ru complexes during photo-activation could also favor the cellular uptake of the compound.

To gain insight into the transport mechanism of the particles, inductively coupled plasma mass spectrometry (ICP-MS) was used to measure the cell-associated Ru content in A549 cells over time under dark conditions (Fig. S33). The results showed that the soluble complex reached its highest cellular Ru level after just one hour of incubation, followed by a rapid decrease, suggesting release from the cells or dissociation, with the implication of potential limitations for tissue retention. In contrast, the particles exhibited slower cellular association, but maintained high levels of cellular Ru over an extended period of time. Both the decline in Ru content from the soluble complex and the accumulation from the particles followed linear trends (Fig. S33). The curves intersected at 24 hours, which coincides with the half-life for release observed in the dark during the dissolution assays. ICP-MS verified the interaction between Ru particles and the cells but did not distinguish whether the Ru materials were adsorbed on the surface, internalized, or both. Accordingly, complementary imaging techniques were employed to precisely localize the distribution of the particles in cells.

Localization of the particles in cells. Complex **1** is emissive with photo-excitation in the MLCT band (λ_{ex} = 453 nm; λ_{em} = 606 nm). Fig. S21 presents the excitation and emission properties of the $[Ru(bpy)_3]Cl_2$ form, as the Cl^- salt is fully soluble in water. The properties of 10 μM aqueous suspensions of the different $[Ru(bpy)_3](PF_6)_2$ particles were also recorded and compared to the fully solubilized $[Ru(bpy)_3]Cl_2$ compound (Fig. S22). The emission spectra of the particles show increased intensity when the size of the particles increased, which could be related to aggregation effects reported previously in the literature.[60,61] Recently, Sheet *et al.*[62] reported the enhancement of emission when increasing the CH_3CN–water mixture ratio due to the spontaneous formation of nanoaggregates in water.

Internalized Ru complexes were localized by treating HeLa cells with compound **1** microparticles then imaging by confocal microscopy (Fig. 3C). The imaging results showed compound **1** emission in both the cytosol and the nucleus. Unfortunately, a comparison between the localization of the soluble complex, the nanoparticles, and the microparticles could not be achieved due to high background signal in the channel used to detect the ruthenium emission. Using image analysis software, the two-dimensional image of the microparticles was converted into 2.5D view, where the signal intensity corresponds to the height in the z-plane. The surface plot shows high intensity foci within the cytoplasm that are indicative of aggregates or intact particles. Diffuse lower intensity signal in the nucleus likely corresponds to the released complex. Together, these results suggest that the particles can be taken up by the cell and the complex can be released in the cytoplasm or nucleus.

To investigate this more deeply, a higher resolution imaging approach was utilized. As compound **1** is a known photosensitizer for the creation of $^1O_2$, it was investigated as a photocatalyst to cause the oxidative polymerization of DAB, which can then be stained with OsO_4[63] (Fig. 4A) for high resolution EM. Previously, genetically engineered fusion proteins with mini-SOG have been used in this way,[37] and the approach provides the complementary and higher resolution imaging than can be achieved with light microscopy.[37] A549 cells were exposed to complex **1**, either as the soluble compound or as particles, to serve as a photocatalyst. After cell fixation, DAB was added, and irradiation of the photocatalyst triggered the production of $^1O_2$ resulting in the polymerization reaction of the DAB. The polymer was then stained with osmium, which allowed for imaging by EM. This process reveals the sites within the cell where the high concentrations of $^1O_2$ were produced, and thus reports on the localization of dissolved **1** species (Fig. S37). Both TEM and STEM were performed on 90 nm thick cross sections and permitted the imaging of the cells with nanoscale resolution, clearly revealing the nucleus and organelles such as mitochondria, liposomes, and Goli apparatus. Polymeric DAB deposits were not observed in the untreated control cells (Fig. 4B), confirming that the presence of Ru was essential for the photocatalytic process.

Cells treated with compound **1** in its solubilized complex form (Fig. S40C and D) exhibited a sparse distribution of micro- and nanoaggregates inside the cells. As mentioned previously, spontaneously formation of aggregates in the stock solution can occur because of the poor solubility of the Ru complex.[62] In addition to the presence of aggregates, diffuse bright spots, attributed to DAB polymeric deposit reveals the localization of the Ru complex in the cytosol. This confirmed the cellular uptake of the compound, either as soluble molecules or microparticles and nanoparticles. For cells treated with FP 1.6 μm particles, intact particles were observed near the cell membrane. Multiple particles were observed within the cell membranes and DAB deposits were observed at the vicinity of the particles, illustrating the dissolution process of the supramolecular structures within

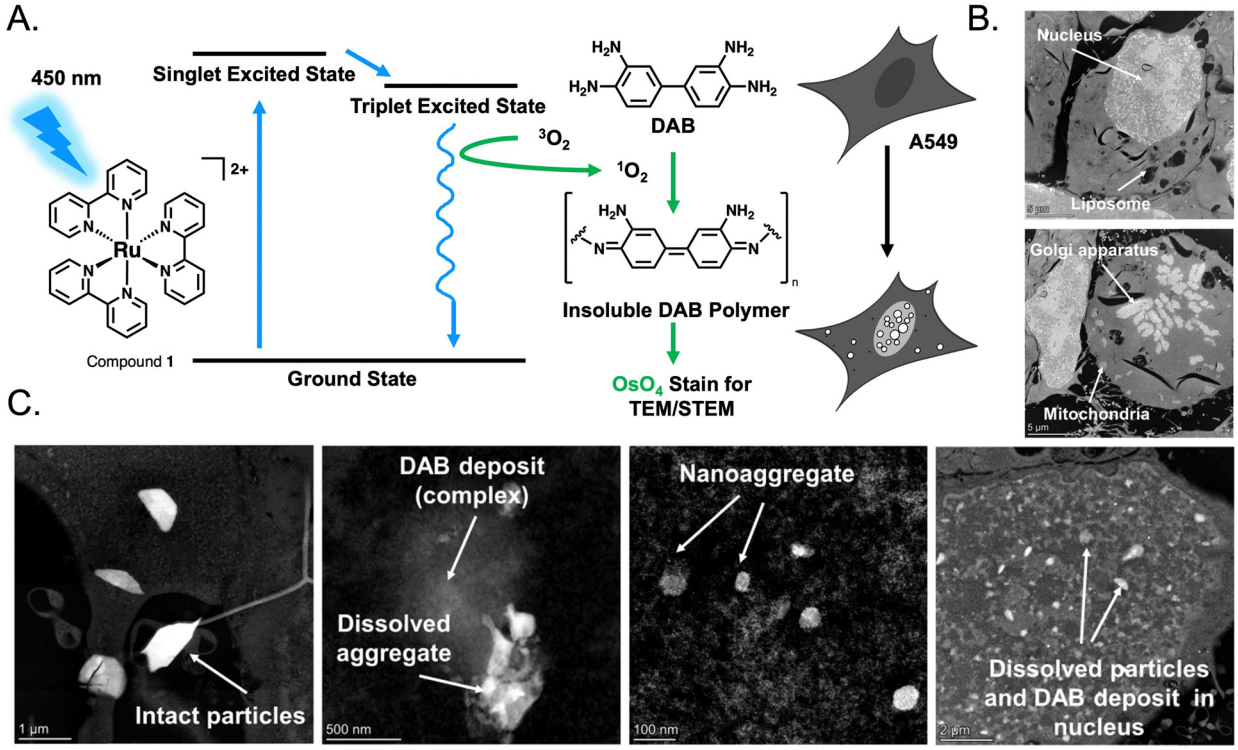

Fig. 4 STEM imaging of compound **1** induced oxidative DAB polymerization in cross sections of A549 cells. (A) Schematic of the sample preparation process: excitation of compound **1** with 450 nm light produces $^1O_2$ that polymerizes the DAB, which is stained with OsO_4 for visualization electron microscopy. The insoluble deposits are formed at the site of the particle. (B) STEM of cells untreated and (C) treated with 20 μM of 1.6 μm particles for 16 hours.

the cytosol and the subsequent release of the Ru complex. These dissolved species were then transported and found in high quantity inside the nucleus of the cells (Fig. 4C). Elemental analysis confirmed the presence of Ru, P, F and Os, characteristic of the Ru compound and staining of DAB with OsO_4. Fig. S38 shows images of the cells treated with 40 nm PVP **1** particles. The biodegradable PVP polymeric films can clearly be seen in different part of the cells including the nucleus and on the cell membrane. The observed polymeric films are composed of 40 nm particles that progressively release Ru over time. However, a substantial number of particles remained embedded in the PVP polymeric matrix, indicating a slower release and accumulation rates compared to the bare 1.6 μm particles. In conclusion, the different formulations of compound **1**, as soluble molecule, bare particles, and as nanocomposites, are all cell permeable. The aggregates and composites dissolve within the cytoplasm and accumulate inside the nucleus, where ROS can be produced upon light irradiation. Moreover, DAB polymerization in the presence of a ROS generator like compound **1** is an efficient way to identify the location of molecules inside the cells using electron microscopy. The particle uptake in cancer cells may be favored by their distinct biological features compared to healthy cells such as an enhanced permeability and retention (EPR) effect leading to a greater accumulation of particles in tumor tissues.[64] This so-called passive targeting could reduce the off-target toxicity of Ru prodrug particles compared to the solubilized form. However, further *in vivo* studies need to be conducted to validate this hypothesis. Finally, one additional benefit of using these systems, especially the pure microparticle forms, is that the materials fully dissolve over time. As a result, they are not anticipated to cause issues associated with long-term micro- and nano-particle accumulation in tissues and organs.[22,23]

Conclusion

We reported a method using the benefits of nanotechnologies to deliver Ru-based compounds in cancer cells. In marked contrast to the approaches mainly used in the literature, this macro-, nano- formulation relies on the growth and transport of Ru complex particles assembled as a supramolecular edifice and forming a ''reservoir'' of molecules, instead of the grafting of single molecules on an external nanocarrier. We showed that the FP technique is particularly suitable and can be applied successfully to cationic Ru(II) polypyridyl complexes to form particles ranging from tens of nanometers to several micrometers. By varying experimental parameters such as the temperature or the presence of a confining agent, we were able to control the particle's size and shape properties. Other parameters not exploited in this study, including but not limited to different solvent/anti-solvent couple and volumes ratio, reaction time, coating agents, could also help to lower the size and modify the properties of the particles, including surface chemistry and charge.

The biological activity of $[Ru(bpy)_3](PF_6)_2$ (compound **1**) and $[Ru(bpy)_2(dmbpy)](PF_6)_2$ (compound **2**) particles were evaluated in HeLa, HL60 and A459 cell lines. Importantly, cytotoxicity data in the dark and after light activation showed similar potencies as the soluble small molecule forms, demonstrating that the particulate forms do not inhibit activity or generate toxicity. Instead, the formation of particles seemed to enhance the cellular association, as revealed by ICP-MS data. Fluorescence and electron microscopy studies revealed that the particle assemblies are easily internalized, and dissolve within the cancer cells to release the complex in the cytosol and nucleus. We also determined that the dissolution rate of the particles is an important feature to evaluate for the stability and the kinetic release of the soluble complex from particles in aqueous medium. The investigation of both PDT and PACT Ru formulations showed that light irradiation can be used for spatiotemporal control of the particle dissolution and release of soluble complex in cells.

This work serves as proof of concept that could be applied to more hydrophobic compounds to prevent premature dissolution of the particles and improve their efficacy. Alternatively, surface functionalization, such as the use of transfecting agents (polymers, proteins, and receptor ligands), could provide a protective shell to the particles, modify the charge, and enhance the target delivery. While the current understanding in the field is that the controlled release of Ru(II) complexes should confer important features to the particles to increase the transport and retention time of Ru complexes *in vivo*, ultimately, the intrinsic benefits of the particle form over soluble molecules would need to be evaluated *in vivo* to confirm the potential of this original approach. However, the simple FP method we detail facilitates the production of hybrid organic–inorganic particles, and the promising *in vitro* results provide proof of efficacy. This report opens new possibilities for pure nanoformulations as an approach towards more effective anticancer metallodrugs for clinical applications.

Conflicts of interest

There are no conflicts to declare.

Abbreviations

PDT	Photodynamic therapy
PACT	Photoactivated chemotherapy
FP	Fast precipitation
bpy	2,2′-Bipyridine
dmbpy	6,6′-Dimethyl-2,2′-bipyridine
$^1O_2$	Singlet oxygen
TEM	Transmission electron microscopy
STEM	Scanning transmission electron microscopy
HAADF	High-angle annular dark-field
EDS	Energy dispersive X-ray
PEG	Polyethylene glycol
PVP	Polyvinylpyrrolidone
DMSO	Dimethyl sulfoxide
FTIR	Fourier transform infrared spectroscopy
DFT	Density functional theory
ATR	Attenuated total reflectance
ξ	Zeta potential
PALS	Phase analysis light scattering
PBS	Phosphate buffered saline
TBS	Tris buffered saline
wt%	Weight percent
MWCO	Molecular weight cut off
UV-Vis	Ultraviolet-visible spectroscopy
EC_{50}	Half maximal effective concentration
OCR	Oxygen consumption rate
FCCP	Carbonyl cyanide 4-(trifluoromethoxy)phenylhydrazone
ROS	Reactive oxygen species
PLR	Poly-L-arginine
PLK	Poly-L-lysine
PLO	Poly-L-ornithine
ICP-MS	Inductively coupled plasma mass spectrometry
DAB	3,3′-diaminobenzidine

Data availability

The data supporting this article have been included as part of the supplementary information (SI). Supplementary information: The SI includes additional experimental details and figures. See DOI: https://doi.org/10.1039/d5tb01785h.

Acknowledgements

We gratefully acknowledge the support of the National Institute of General Medical Sciences of the National Institutes of Health under Award Numbers R01GM138882 and R01GM107586 and the National Science Foundation (CHE-2333820).

References

1 O. C. Farokhzad and R. Langer, Impact of Nanotechnology on Drug Delivery, *ACS Nano*, 2009, **3**(1), 16–20, DOI: 10.1021/nn900002m.
2 M. J. Mitchell, M. M. Billingsley, R. M. Haley, M. E. Wechsler, N. A. Peppas and R. Langer, Engineering Precision Nanoparticles for Drug Delivery, *Nat. Rev. Drug Discovery*, 2021, **20**(2), 101–124, DOI: 10.1038/s41573-020-0090-8.
3 L. Zeng, P. Gupta, Y. Chen, E. Wang, L. Ji, H. Chao and Z.-S. Chen, The Development of Anticancer Ruthenium(II) Complexes: From Single Molecule Compounds to Nanomaterials, *Chem. Soc. Rev.*, 2017, **46**(19), 5771–5804, DOI: 10.1039/C7CS00195A.
4 N. Soliman, G. Gasser and C. M. Thomas, Incorporation of Ru(II) Polypyridyl Complexes into Nanomaterials for Cancer Therapy and Diagnosis, *Adv. Mater.*, 2020, **32**(47), 2003294, DOI: 10.1002/adma.202003294.
5 J. Shen, T. W. Rees, L. Ji and H. Chao, Recent Advances in Ruthenium(II) and Iridium(III) Complexes Containing Nanosystems for Cancer Treatment and Bioimaging, *Coord.*

Chem. Rev., 2021, **443**, 214016, DOI: 10.1016/j.ccr.2021.214016.

6 Y. Lu, D. Zhu, Q. Le, Y. Wang and W. Wang, Ruthenium-Based Antitumor Drugs and Delivery Systems from Monotherapy to Combination Therapy, *Nanoscale*, 2022, **14**(44), 16339–16375, DOI: 10.1039/d2nr02994d.

7 M. Dickerson, B. Howerton, Y. Bae and E. C. Glazer, Light-Sensitive Ruthenium Complex-Loaded Cross-Linked Polymeric Nanoassemblies for the Treatment of Cancer, *J. Mater. Chem. B*, 2016, **4**(3), 394–408, DOI: 10.1039/C5TB01613D.

8 E. Villemin, Y. C. Ong, C. M. Thomas and G. Gasser, Polymer Encapsulation of Ruthenium Complexes for Biological and Medicinal Applications, *Nat. Rev. Chem.*, 2019, **3**(4), 261–282, DOI: 10.1038/s41570-019-0088-0.

9 J. Karges, J. Li, L. Zeng, H. Chao and G. Gasser, Polymeric Encapsulation of a Ruthenium Polypyridine Complex for Tumor Targeted One- and Two-Photon Photodynamic Therapy, *ACS Appl. Mater. Interfaces*, 2020, **12**(49), 54433–54444, DOI: 10.1021/acsami.0c16119.

10 B. Purushothaman, J. Lee, S. Hong and J. M. Song, Multifunctional TPP-PEG-Biotin Self-Assembled Nanoparticle Drug Delivery-Based Combination Therapeutic Approach for Co-Targeting of GRP78 and Lysosome, *J. Nanobiotechnol.*, 2020, **18**(1), 102, DOI: 10.1186/s12951-020-00661-y.

11 M. Fandzloch, A. Jaromin, M. Zaremba-Czogalla, A. Wojtczak, A. Lewińska, J. Sitkowski, J. Wiśniewska, I. Łakomska and J. Gubernator, Nanoencapsulation of a Ruthenium(II) Complex with Triazolopyrimidine in Liposomes as a Tool for Improving Its Anticancer Activity against Melanoma Cell Lines, *Dalton Trans.*, 2020, **49**(4), 1207–1219, DOI: 10.1039/C9DT03464A.

12 D. Sun, Y. Liu, Q. Yu, X. Qin, L. Yang, Y. Zhou, L. Chen and J. Liu, Inhibition of Tumor Growth and Vasculature and Fluorescence Imaging Using Functionalized Ruthenium-Thiol Protected Selenium Nanoparticles, *Biomaterials*, 2014, **35**(5), 1572–1583, DOI: 10.1016/j.biomaterials.2013.11.007.

13 Y. Ellahioui, M. Patra, C. Mari, R. Kaabi, J. Karges, G. Gasser and S. Gómez-Ruiz, Mesoporous Silica Nanoparticles Functionalised with a Photoactive Ruthenium(II) Complex: Exploring the Formulation of a Metal-Based Photodynamic Therapy Photosensitiser, *Dalton Trans.*, 2019, **48**(18), 5940–5951, DOI: 10.1039/C8DT02392A.

14 Y.-K. Dou, Y. Shang, X.-W. He, W.-Y. Li, Y.-H. Li and Y.-K. Zhang, Preparation of a Ruthenium-Complex-Functionalized Two-Photon-Excited Red Fluorescence Silicon Nanoparticle Composite for Targeted Fluorescence Imaging and Photodynamic Therapy in Vitro, *ACS Appl. Mater. Interfaces*, 2019, **11**(15), 13954–13963, DOI: 10.1021/acsami.9b00288.

15 S. Estalayo-Adrián, G. J. McManus, H. L. Dalton, A. J. Savyasachi, J. M. Kelly and T. Gunnlaugsson, Functionalisation of Gold Nanoparticles with Ruthenium(II) Polypyridyl Complexes for Their Application in Cellular Imaging, *Dalton Trans.*, 2020, **49**(40), 14158–14168, DOI: 10.1039/D0DT02754E.

16 M. S. Meijer, M. M. Natile and S. Bonnet, 796 Nm Activation of a Photocleavable Ruthenium(II) Complex Conjugated to an Upconverting Nanoparticle through Two Phosphonate Groups, *Inorg. Chem.*, 2020, **59**(20), 14807–14818, DOI: 10.1021/acs.inorgchem.0c00043.

17 A. N. Dosumu, S. Claire, L. S. Watson, P. M. Girio, S. A. M. Osborne, Z. Pikramenou and N. J. Hodges, Quantification by Luminescence Tracking of Red Emissive Gold Nanoparticles in Cells, *JACS Au*, 2021, **1**(2), 174–186, DOI: 10.1021/jacsau.0c00033.

18 D.-Y. Zhang, Y. Zheng, H. Zhang, L. He, C.-P. Tan, J.-H. Sun, W. Zhang, X. Peng, Q. Zhan, L.-N. Ji and Z.-W. Mao, Ruthenium Complex-Modified Carbon Nanodots for Lysosome-Targeted One- and Two-Photon Imaging and Photodynamic Therapy, *Nanoscale*, 2017, **9**(47), 18966–18976, DOI: 10.1039/C7NR05349E.

19 P. Zhang, H. Huang, J. Huang, H. Chen, J. Wang, K. Qiu, D. Zhao, L. Ji and H. Chao, Noncovalent Ruthenium(II) Complexes–Single-Walled Carbon Nanotube Composites for Bimodal Photothermal and Photodynamic Therapy with Near-Infrared Irradiation, *ACS Appl. Mater. Interfaces*, 2015, **7**(41), 23278–23290, DOI: 10.1021/acsami.5b07510.

20 D.-Y. Zhang, Y. Zheng, C.-P. Tan, J.-H. Sun, W. Zhang, L.-N. Ji and Z.-W. Mao, Graphene Oxide Decorated with Ru(II)–Polyethylene Glycol Complex for Lysosome-Targeted Imaging and Photodynamic/Photothermal Therapy, *ACS Appl. Mater. Interfaces*, 2017, **9**(8), 6761–6771, DOI: 10.1021/acsami.6b13808.

21 C. Riccardi, D. Musumeci, M. Trifuoggi, C. Irace, L. Paduano and D. Montesarchio, Anticancer Ruthenium(III) Complexes and Ru(III)-Containing Nanoformulations: An Update on the Mechanism of Action and Biological Activity, *Pharmaceuticals*, 2019, **12**(4), 146, DOI: 10.3390/ph12040146.

22 R. Mohammadpour, M. A. Dobrovolskaia, D. L. Cheney, K. F. Greish and H. Ghandehari, Subchronic and Chronic Toxicity Evaluation of Inorganic Nanoparticles for Delivery Applications, *Adv. Drug Delivery Rev.*, 2019, **144**, 112–132, DOI: 10.1016/j.addr.2019.07.006.

23 D. Havrylyuk, D. K. Heidary and E. C. Glazer, The Impact of Inorganic Systems and Photoactive Metal Compounds on Cytochrome P450 Enzymes and Metabolism: From Induction to Inhibition, *Biomolecules*, 2024, **14**(4), 441, DOI: 10.3390/biom14040441.

24 A. Notaro, G. Gasser and A. Castonguay, Note of Caution for the Aqueous Behaviour of Metal-Based Drug Candidates, *ChemMedChem*, 2020, **15**(4), 345–348, DOI: 10.1002/cmdc.201900677.

25 B. Siewert, M. Langerman, Y. Hontani, J. T. M. Kennis, V. H. S. Van Rixel, B. Limburg, M. A. Siegler, V. Talens Saez, R. E. Kieltyka and S. Bonnet, Turning on the Red Phosphorescence of a [Ru(Tpy)(Bpy)(Cl)]Cl Complex by Amide Substitution: Self-Aggregation, Toxicity, and Cellular Localization of an Emissive Ruthenium-Based Amphiphile, *Chem. Commun.*, 2017, **53**(81), 11126–11129, DOI: 10.1039/c7cc02989f.

26 W. Sun, S. Li, B. Häupler, J. Liu, S. Jin, W. Steffen, U. S. Schubert, H. Butt, X. Liang and S. Wu, An Amphiphilic Ruthenium Polymetallodrug for Combined Photodynamic Therapy and Photochemotherapy In Vivo, *Adv. Mater.*, 2017, **29**(6), DOI: 10.1002/adma.201603702.

27 H. Xu, X. Zhang, X. Li, X. Zhang, J. Deng, D. Zou and J. Yang, Two Ru(II) Compounds with Aggregation Induced Emission as Promising Photosensitizers for Photodynamic Therapy, *J. Inorg. Biochem.*, 2020, **212**, 111233, DOI: 10.1016/j.jinorgbio.2020.111233.
28 J. Yang, X. He, Z. Ke, J. Chen, Z. Zou, B. Wei, D. Zou and J. Zou, Two Photoactive Ru (II) Compounds Based on Tetrazole Ligands for Photodynamic Therapy, *J. Inorg. Biochem.*, 2020, **210**, 111127, DOI: 10.1016/j.jinorgbio.2020.111127.
29 X. Zhang, X. Huang, A. Xie, X. Zhang, J. Deng, D. Zou and J. Zou, Boosting Type I Process of Ru(II) Compounds by Changing Tetrazole Ligand for Enhanced Photodynamic Therapy against Lung Cancer, *J. Inorg. Biochem.*, 2020, **212**, 111236, DOI: 10.1016/j.jinorgbio.2020.111236.
30 R. Zhang, X. Fan, Z. Meng, H. Lin, Q. Jin, F. Gong, Z. Dong, Y. Li, Q. Chen, Z. Liu and L. Cheng, Renal Clearable Ru-Based Coordination Polymer Nanodots for Photoacoustic Imaging Guided Cancer Therapy, *Theranostics*, 2019, **9**(26), 8266–8276, DOI: 10.7150/thno.36986.
31 A. Carné, C. Carbonell, I. Imaz and D. Maspoch, Nanoscale Metal–Organic Materials, *Chem. Soc. Rev.*, 2011, **40**(1), 291–305, DOI: 10.1039/c0cs00042f.
32 L. L. Nguyen, R. Guillot, J. Laisney, L. Rechignat, S. Bedoui, G. Molnár, E. Rivière and M.-L. Boillot, Fe(Me_2 -Bpy)$_2$ ($NCSe)_2$ Spin-Crossover Micro- and Nanoparticles Showing Spin-State Switching above 250 K, *New J. Chem.*, 2015, **39**(3), 1603–1610, DOI: 10.1039/C4NJ01257G.
33 J. Laisney, A. Tissot, G. Molnár, L. Rechignat, E. Rivière, F. Brisset, A. Bousseksou and M.-L. Boillot, Nanocrystals of Fe(Phen)$_2$ ($NCS)_2$ and the Size-Dependent Spin-Crossover Characteristics, *Dalton Trans.*, 2015, **44**(39), 17302–17311, DOI: 10.1039/C5DT02840J.
34 A. Tissot, L. Rechignat, A. Bousseksou and M.-L. Boillot, Micro- and Nanocrystals of the Iron(III) Spin-Transition Material [FeIII(3-MeO-SalEen)2]PF6, *J. Mater. Chem.*, 2012, **22**(8), 3411, DOI: 10.1039/c2jm14913c.
35 F. P. Dwyer, E. C. Gyarfas, W. P. Rogers and J. H. Koch, Biological Activity of Complex Ions, *Nature*, 1952, **170**(4318), 190–191, DOI: 10.1038/170190a0.
36 Y. Sun, D. K. Heidary, Z. Zhang, C. I. Richards and E. C. Glazer, Bacterial Cytological Profiling Reveals the Mechanism of Action of Anticancer Metal Complexes, *Mol. Pharm.*, 2018, **15**(8), 3404–3416, DOI: 10.1021/acs.molpharmaceut.8b00407.
37 X. Shu, V. Lev-Ram, T. J. Deerinck, Y. Qi, E. B. Ramko, M. W. Davidson, Y. Jin, M. H. Ellisman and R. Y. Tsien, A Genetically Encoded Tag for Correlated Light and Electron Microscopy of Intact Cells, Tissues, and Organisms, *PLoS Biol.*, 2011, **9**(4), e1001041, DOI: 10.1371/journal.pbio.1001041.
38 A. Rodríguez-Pulido, A. L. Cortajarena, J. Torra, R. Ruiz-González, S. Nonell and C. Flors, Assessing the Potential of Photosensitizing Flavoproteins as Tags for Correlative Microscopy, *Chem. Commun.*, 2016, **52**(54), 8405–8408, DOI: 10.1039/C6CC03119F.
39 T. C. Binns, A. X. Ayala, J. B. Grimm, A. N. Tkachuk, G. A. Castillon, S. Phan, L. Zhang, T. A. Brown, Z. Liu, S. R. Adams, M. H. Ellisman, M. Koyama and L. D. Lavis, Rational Design of Bioavailable Photosensitizers for Manipulation and Imaging of Biological Systems, *Cell Chem. Biol.*, 2020, **27**(8), 1063–1072, DOI: 10.1016/j.chembiol.2020.07.001.
40 B. S. Howerton, D. K. Heidary and E. C. Glazer, Strained Ruthenium Complexes Are Potent Light-Activated Anticancer Agents, *J. Am. Chem. Soc.*, 2012, **134**(20), 8324–8327, DOI: 10.1021/ja3009677.
41 A. M. Schrand, J. J. Schlager, L. Dai and S. M. Hussain, Preparation of Cells for Assessing Ultrastructural Localization of Nanoparticles with Transmission Electron Microscopy, *Nat. Protoc.*, 2010, **5**(4), 744–757, DOI: 10.1038/nprot.2010.2.
42 V. K. LaMer and R. H. Dinegar, Theory, Production and Mechanism of Formation of Monodispersed Hydrosols, *J. Am. Chem. Soc.*, 1950, **72**(11), 4847–4854, DOI: 10.1021/ja01167a001.
43 K. Knop, R. Hoogenboom, D. Fischer and U. S. Schubert, Poly(Ethylene Glycol) in Drug Delivery: Pros and Cons as Well as Potential Alternatives, *Angew. Chem., Int. Ed.*, 2010, **49**(36), 6288–6308, DOI: 10.1002/anie.200902672.
44 X. Liu, Y. Xu, Z. Wu and H. Chen, Poly(*N* -vinylpyrrolidone)-Modified Surfaces for Biomedical Applications, *Macromol. Biosci.*, 2013, **13**(2), 147–154, DOI: 10.1002/mabi.201200269.
45 M. Anbarasu, M. Anandan, E. Chinnasamy, V. Gopinath and K. Balamurugan, Synthesis and Characterization of Polyethylene Glycol (PEG) Coated Fe3O4 Nanoparticles by Chemical Co-Precipitation Method for Biomedical Applications, *Spectrochim. Acta, Part A*, 2015, **135**, 536–539, DOI: 10.1016/j.saa.2014.07.059.
46 M. A. Tshabalala, B. F. Dejene and H. C. Swart, Synthesis and Characterization of ZnO Nanoparticles Using Polyethylene Glycol (PEG, *Phys. B*, 2012, **407**(10), 1668–1671, DOI: 10.1016/j.physb.2011.09.113.
47 K. M. Koczkur, S. Mourdikoudis, L. Polavarapu and S. E. Skrabalak, Polyvinylpyrrolidone (PVP) in Nanoparticle Synthesis, *Dalton Trans.*, 2015, **44**(41), 17883–17905, DOI: 10.1039/C5DT02964C.
48 G. Prencipe, S. M. Tabakman, K. Welsher, Z. Liu, A. P. Goodwin, L. Zhang, J. Henry and H. Dai, PEG Branched Polymer for Functionalization of Nanomaterials with Ultralong Blood Circulation, *J. Am. Chem. Soc.*, 2009, **131**(13), 4783–4787, DOI: 10.1021/ja809086q.
49 Y. Kaneda, Y. Tsutsumi, Y. Yoshioka, H. Kamada, Y. Yamamoto, H. Kodaira, S. Tsunoda, T. Okamoto, Y. Mukai, H. Shibata, S. Nakagawa and T. Mayumi, The Use of PVP as a Polymeric Carrier to Improve the Plasma Half-Life of Drugs, *Biomaterials*, 2004, **25**(16), 3259–3266, DOI: 10.1016/j.biomaterials.2003.10.003.
50 B. A. Rozenberg and R. Tenne, Polymer-Assisted Fabrication of Nanoparticles and Nanocomposites, *Prog. Polym. Sci.*, 2008, **33**(1), 40–112, DOI: 10.1016/j.progpolymsci.2007.07.004.
51 P. K. Mallick, G. D. Danzer, D. P. Strommen and J. R. Kincaid, Vibrational Spectra and Normal-Coordinate Analysis of Tris(Bipyridine)Ruthenium(II, *J. Phys. Chem.*, 1988, **92**(20), 5628–5634, DOI: 10.1021/j100331a018.
52 B. D. Alexander, T. J. Dines and R. W. Longhurst, DFT Calculations of the Structures and Vibrational Spectra of the [Fe(Bpy)3]2+ and [Ru(Bpy)3]2+ Complexes, *Chem. Phys.*, 2008, **352**(1–3), 19–27, DOI: 10.1016/j.chemphys.2008.05.010.

53 J. Polte, Fundamental Growth Principles of Colloidal Metal Nanoparticles – a New Perspective, *CrystEngComm*, 2015, **17**(36), 6809–6830, DOI: 10.1039/C5CE01014D.
54 B. Kuttich, A. Matt, C. Appel and B. Stühn, X-Ray Scattering Study on the Crystalline and Semi-Crystalline Structure of Water/PEG Mixtures in Their Eutectic Phase Diagram, *Soft Matter*, 2020, **16**(45), 10260–10267, DOI: 10.1039/D0SM01601B.
55 R. J. Mitchell, D. Havrylyuk, A. C. Hachey, D. K. Heidary and E. C. Glazer, Photodynamic Therapy Photosensitizers and Photoactivated Chemotherapeutics Exhibit Distinct Bioenergetic Profiles to Impact ATP Metabolism, *Chem. Sci.*, 2025, **16**(2), 721–734, DOI: 10.1039/D4SC05393A.
56 J. Zanzi, Z. Pastorel, C. Duhayon, E. Lognon, C. Coudret, A. Monari, I. M. Dixon, Y. Canac, M. Smietana and O. Baslé, Counterion Effects in $[Ru(Bpy)_3](X)_2$ -Photocatalyzed Energy Transfer Reactions, *JACS Au*, 2024, **4**(8), 3049–3057, DOI: 10.1021/jacsau.4c00384.
57 U. Lächelt and E. Wagner, Nucleic Acid Therapeutics Using Polyplexes: A Journey of 50 Years (and Beyond, *Chem. Rev.*, 2015, **115**(19), 11043–11078, DOI: 10.1021/cr5006793.
58 B. Collin, E. Oostveen, O. V. Tsyusko and J. M. Unrine, Influence of Natural Organic Matter and Surface Charge on the Toxicity and Bioaccumulation of Functionalized Ceria Nanoparticles in *Caenorhabditis Elegans*, *Environ. Sci. Technol.*, 2014, **48**(2), 1280–1289, DOI: 10.1021/es404503c.
59 S. Behzadi, V. Serpooshan, W. Tao, M. A. Hamaly, M. Y. Alkawareek, E. C. Dreaden, D. Brown, A. M. Alkilany, O. C. Farokhzad and M. Mahmoudi, Cellular Uptake of Nanoparticles: Journey inside the Cell, *Chem. Soc. Rev.*, 2017, **46**(14), 4218–4244, DOI: 10.1039/C6CS00636A.
60 Y. Chen, W.-C. Xu, J.-F. Kou, B.-L. Yu, X.-H. Wei, H. Chao and L.-N. Ji, Aggregation-Induced Emission of Ruthenium(II) Polypyridyl Complex [Ru(Bpy)2(Pzta)]2+, *Inorg. Chem. Commun.*, 2010, **13**(10), 1140–1143, DOI: 10.1016/j.inoche.2010.06.029.
61 E. Babu, P. M. Mareeswaran, M. M. Krishnan, V. Sathish, P. Thanasekaran and S. Rajagopal, Unravelling the Aggregation Induced Emission Enhancement in Tris(4,7-Diphenyl-1,10-Phenanthroline)Ruthenium(II) Complex, *Inorg. Chem. Commun.*, 2018, **98**, 7–10, DOI: 10.1016/j.inoche.2018.09.035.
62 S. K. Sheet, B. Sen, S. K. Patra, M. Rabha, K. Aguan and S. Khatua, Aggregation-Induced Emission-Active Ruthenium(II) Complex of 4,7-Dichloro Phenanthroline for Selective Luminescent Detection and Ribosomal RNA Imaging, *ACS Appl. Mater. Interfaces*, 2018, **10**(17), 14356–14366, DOI: 10.1021/acsami.7b19290.
63 A. M. Seligman, M. J. Karnovsky, H. L. Wasserkrug and J. S. Hanker, Nanodroplet Ultrastructural Demonstration of Cytochrome Oxidase Activity with a Polymerizing Osmiophilic Reagent, Diaminobenzidine (DAB), *J. Cell Biol.*, 1968, **38**(1), 1–14, DOI: 10.1083/jcb.38.1.1.
64 I.-A. Vagena, C. Malapani, M.-A. Gatou, N. Lagopati and E. A. Pavlatou, Enhancement of EPR Effect for Passive Tumor Targeting: Current Status and Future Perspectives, *Appl. Sci.*, 2025, **15**(6), 3189, DOI: 10.3390/app15063189.

